compared to the BE of 3.85 eV/atom for Si_{10}, and therefore the stability of Si_{10} cluster is enhanced by Ni doping (Table 1).

Doping of Pd in Si_{10} is favored outside (Figure 2a) with 1.70 eV HOMO−LUMO gap. A 3-fold structure (Figure 1c) lies 1.03 eV higher in energy with a 1.27 eV HOMO−LUMO gap. A decahedron with Pd inside opens up (Figure 2b). It lies 1.13 eV higher in energy with a HOMO−LUMO gap of 1.79 eV. It is to be noted that a similar structure for Ni lies 0.77 eV higher in energy than the lowest energy structure as the strain is reduced. A decahedron with 2 μ_B magnetic moment lies 1.5 eV higher in energy with a small HOMO−LUMO gap of 0.32 eV. Lu and Nagase[13] studied Os doping in Si_{10} and Ge_{10} and obtained open structures, showing that Os is not appropriate. The capped square antiprism structure converges to a slightly distorted (one square face becoming rectangular) decahedron. This structure lies 1.53 eV higher in energy with 1.34 eV HOMO−LUMO gap. The pentagon-rhombus isomer (Figure 1a) is almost degenerate with a 3-fold isomer (Figure 1b) and lies 1.71 eV higher in energy. These results show that Pd doping is unlikely inside Si_{10} as the gain in energy is only 2.48 eV. Outside doping may be possible with the energy gain of 3.49 eV.

The case of $Si_{10}Pt$ is, however, different. The lowest energy structure is a 3-fold isomer (Figure 1c). An isomer in which Pt opens the cage (Figure 2b) and is exposed for reactivity lies only 0.14 eV higher in energy. It also has a significant HOMO−LUMO gap of 1.32 eV. A capped square antiprism and a pentagonal antiprism also converge to this isomer. This isomer has rhombi in abundance. This tendency is also seen in another rather open structure (Figure 2c) which lies 0.41 eV higher in energy with 1.23 eV gap. A decahedron is stable with a magnetic moment of 2 μ_B and lies 0.57 eV higher in energy, similar to the case of Ni. The capped pentagon-rhombus structure lies 0.90 eV higher in energy with a significant gap of 1.67 eV and is very close to having 3-fold symmetry. Therefore, Pt doping is different from Ni and Pd. The gain in energy by Pt doping in the lowest energy structure is 4.83 eV and therefore, it also enhances the stability of Si_{10} but the HOMO−LUMO gap is significantly reduced to 1.29 eV as compared to 2.09 eV for Si_{10}.

As the atomic size of Ge is about 4% bigger than Si, the lowest energy structure of $Ge_{10}Ni$ is a capped square antiprism (Figure 1d), in contrast to the Si case for which it is unstable. The HOMO−LUMO gap is 1.66 eV, which is the highest among all the geometries studied for this cluster but smaller than the value for Ge_{10}. A bicapped cube also converges to this structure. A TTP structure (Figure 1b) is nearly degenerate and has a 1.67 eV HOMO−LUMO gap. The next lowest energy structure is decahedral and it lies 1.37 eV higher in energy with 2 μ_B magnetic moment. Ni atom is the optimal to stabilize this closed cage structure with very little elongation in Ge−Ge bond lengths as compared to the Ge_{10} cluster. The Ge−Ni bonds are shorter (2.44 Å) than the sum of the covalent radii of Ge and Ni. Therefore, it has significantly higher BE as compared to other isomers. The energy gain by Ni doping is 5.56 eV similar to silicon. However, the BE of Ge clusters is significantly lower as compared to Si clusters, and therefore the improvement in stabilization is more significant (Table 1), which makes it exceptional.

To optimize the HOMO−LUMO gap and the effect of the size of the dopant in the same group, we further studied $Ge_{10}Pd$ in different geometries. The lowest energy structure is similar to $Si_{10}Ni$ (Figure 1a) and the energy gain is 3.26 eV, which is more than the value for the Si cage as the strain in Ge is reduced. Therefore, going down from Si to Ge and Ni to Pd in the same column retains similar behavior, but the BE in the case of Pd decreases due to its closed shell atomic electronic structure. The TTP structure also converges to this isomer. Another isomer in which Pd is outside the Ge_{10} cluster (Figure 2a) is nearly degenerate while a distorted structure and the 3-fold symmetric structure (Figure 1c) lie 0.30 eV higher in energy. Therefore, Pd doping in Ge_{10} is not favorable as it is also the case for Si_{10}. Continuing further with $Ge_{10}Pt$, we find that the lowest energy structure is the same as for $Ge_{10}Pd$ (Figure 1a). However, the gain in energy of Ge_{10} due to doping is 5.26 eV. The hybridization of Pt orbitals with those of the Ge cage is better and it enhances the stability of Ge_{10}. The HOMO−LUMO gap in this case is 1.54 eV and similar to $Ge_{10}Ni$; this cluster should be strongly abundant. The Ge−Ge and Ge−Pt bond lengths increase by about 4% as compared to Ge_{10}. But the similar gain in energy as for Ni shows that the interaction of Pt with the cage is stronger. The 3-fold symmetric structure (Figure 1c) is nearly degenerate (0.08 eV higher) with 1.08 eV gap. The energy difference from the second lowest energy structure (Figure 1d) decreases to 0.39 eV while Pt outside Ge_{10} lies 0.54 eV higher in energy as compared to the lowest energy isomer. Therefore, Pt encapsulation also enhances the stability of Ge_{10} significantly.

Next we studied $Sn_{10}M$ (M = Ni, Pd, and Pt) clusters. Sn is significantly larger as compared to Si or Ge and has a tendency to be more metallic. Therefore, several of the structures (Figure 1a, b, and d) become nearly degenerate. The lowest energy structure for $Sn_{10}Ni$ is a bicapped square antiprism (Figure 1d) with a 1.23 eV HOMO−LUMO gap, which is slightly smaller as compared to the value for Sn_{10}. A 3-fold symmetric structure (Figure 1b) with slight distortion and the capped pentagonal-rhombus structure (Figure 1a) each lie only 0.06 eV higher in energy. Ni outside Sn_{10} lies 2.20 eV higher in energy. The same happens for Pd and Pt. Among these, the HOMO−LUMO gap is the largest (1.30 eV) for $Sn_{10}Pt$ in the lowest energy bicapped square antiprism structure. In this case also the Sn−Sn bond lengths are nearly the same as in Sn_{10} and so the strain due to doping is minimal. A similar trend is observed for Pb. The lowest energy structure for all M is a bicapped square antiprism (Figure 1e). In the case of Ni the HOMO−LUMO gap decreases to 0.84 as Ni is small and is not optimally bonded. But it increases to 0.99 eV for Pd and further to 1.06 eV for Pt. Therefore, we conclude that Pt is also the most optimally bonded in this case. The Pb−Pb bond lengths remain also nearly the same as in the lowest energy structure of Pb_{10}. This is also reflected from the energy gain which is 6.58

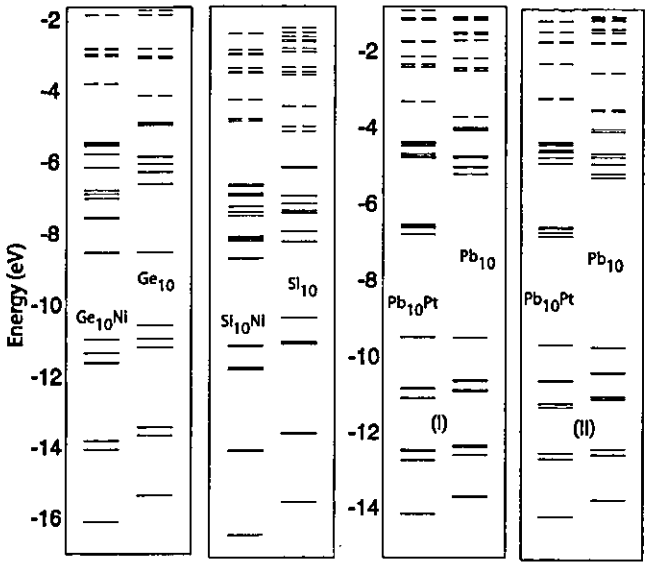

Figure 3. Kohn-Sham electronic states for different $X_{10}M$ and X_{10} (with the corresponding atomic positions) clusters. (I) and (II) are for the bicapped square antiprism and tetracapped trigonal prism isomers of $Pb_{10}Pt$, respectively.

and 6.52 eV for Sn and Pb, respectively. The gain in energy with Pd doping is 4.49 and 4.56 eV for Sn_{10} and Pb_{10}, respectively, while for Ni it is 5.54 and 5.21 eV, making Pt to be the best dopant for Sn_{10} and Pb_{10}.

These results show that Ni doped Si_{10} and Ge_{10}, and Pt doped Ge_{10}, Sn_{10}, and Pb_{10} clusters are optimal and are among the smallest TM atom encapsulated caged magic clusters of these tetravalent elements known so far. To understand the bonding nature we have shown in Figure 3 the Kohn–Sham energy states of the doped and undoped clusters keeping the same atomic configuration of the X atoms as in the doped cases. It is clear that most of the occupied states shift slightly to higher binding energies after doping, indicating that there could be small transfer of charge from the cage (Figure 4). The HOMO–LUMO gap for the distorted X_{10} cages reduces significantly as compared to the lowest energy structures. However, the states near the HOMO are significantly pushed down, whereas the LUMO of the X_{10} cage gets shifted upward, giving rise to a large gap as well as significant gain in energy leading to the stability of these clusters. Also comparing the states of X_{10} and $X_{10}M$ clusters, the covalently bonded d level of the TM atom forms the HOMO and is fully occupied. This supports our conjecture of the closed electronic d level in these magic clusters.

The electronic charge densities are shown in Figure 4 for the lowest energy structures of $Ge_{10}Ni$, $Si_{10}Ni$, and $Pb_{10}Pt$ clusters, which are among the best representative cases. The values of the isosurfaces have been kept to be the same in all cases for comparison. It is seen from the difference in the charge densities of the doped clusters and the overlapping densities of M and X_{10} with the corresponding positions as in $M@X_{10}$ that the charge is accumulated between the M atom and the X_{10} cage due to the covalent bonding. As we go down in the X column from Si to Pb, the charge accumulation decreases due to the more metallic character of bonding in these clusters. This is also reflected from the

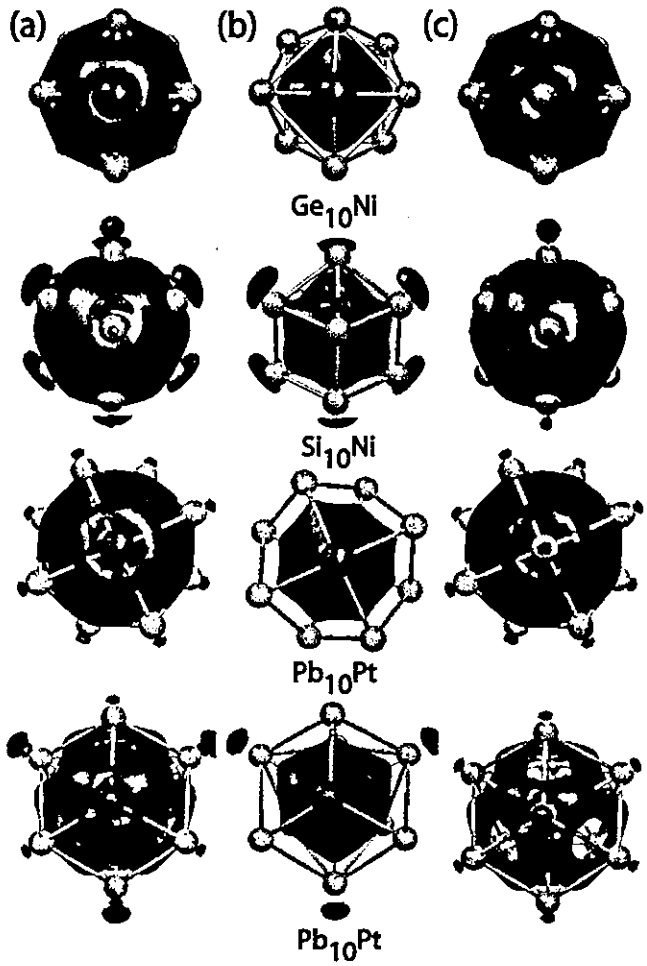

Figure 4. (a) Isosurface for the accumulation (red) and depletion (blue) of the electronic charge in $X_{10}M$ as compared to the isolated M and X_{10} with the same positions. Set (b) shows accumulation and (c) shows the depletion of charge separately.

reduction in the depletion of charge from the X_{10} cage as well as smaller shift in the electronic states of $Pb_{10}M$ clusters (Figure 3).

In summary, we have systematically studied the $X_{10}M$ (X = Si, Ge, Sn, and Pb; M = Ni, Pd, and Pt) clusters and found some of the optimally M doped smallest magic clusters of the group 14 elements with 10 atoms. The stability of these clusters has been understood. We find that by suitably choosing X and M, the properties of these clusters can be tailored to optimize the stability as well as the HOMO–LUMO gap. $Si_{10}Ni$ shows the highest HOMO–LUMO gap of 1.96 eV, and this could be luminescent in the visible range. Sn and Pb clusters have the maximum stabilization energy. As we move down the group from Si to Pb, the enhancement in the stability of caged structures increases more by doping a bigger atom, such as Pt, because the strain due to the small size of the cage is reduced. Our results explain the stability and large abundances of $Ge_{10}Co^-$ clusters also while the best candidates for neutral clusters have been identified. These magic clusters with enhanced stabilities are likely to be produced in large quantities and can be used for making the assemblies of such clusters for nanoscale applications.

Acknowledgment. The authors thank the staff of the Center for Computational Material Science at the Institute for Materials Research for the use of Hitachi SR8000/64 supercomputing facilities. A.K.S. is grateful for the support of MEXT fellowship. V.K. acknowledges the hospitality at the Laboratory for Advanced Materials of the Institute for Materials Research.

References

(1) Kumar, V.; Kawazoe, Y. *Phys. Rev. Lett.* **2001**, *87*, 045503. Kumar, V.; Kawazoe, Y. *Phys. Rev. Lett.* **2003**, *91*, 199901 (E). Kumar, V. *Eur. Phys. J. D* **2003**, *24*, 227.
(2) Kumar, V.; Kawazoe, Y. *Phys. Rev. Lett.* **2002**, *88*, 235504.
(3) Kumar, V.; Kawazoe, Y. *Phys. Rev. B* **2002**, *65*, 073404.
(4) Kumar, V.; Kawazoe, Y. *Phys. Rev. Lett.* **2003**, *90*, 055502.
(5) Kumar, V.; Kawazoe, Y. *Appl. Phys. Lett.* **2002**, *80*, 859.
(6) Hiura, H.; Miyazaki, T.; Kanayama, T. *Phys. Rev. Lett.* **2001**, *86*, 1733.
(7) Kumar, V.; Briere, T. M.; Kawazoe, Y. *Phys. Rev. B* **2003**, *68*, 155412.
(8) Singh, A. K.; Kumar, V.; Briere, T. M.; Kawazoe, Y. *Nano Lett.* **2002**, *2*, 1243.
(9) Singh, A. K.; Briere, T. M.; Kumar, V.; Kawazoe, Y. *Phys. Rev. Lett.* **2003**, *91*, 146802.
(10) Singh, A. K.; Kumar, V.; Kawazoe, Y. *J. Mater. Chem.* **2004**, *14*, 555.
(11) Singh, A. K.; Kumar, V.; Kawazoe, Y., submitted for publication.
(12) Ohara, M.; Koyasu, K.; Nakajima, A.; Kaya, K. *Chem. Phys. Lett.* **2003**, *371*, 490.
(13) Lu, J.; Nagase, S. *Phys. Rev. Lett.* **2003**, *90*, 115506. Khanna, S. N.; Rao, B. K.; Jena, P.; Nayak, S. K. *Chem. Phys. Lett.* **2003**, *373*, 433. Lu, J.; Nagase, S. *Chem. Phys. Lett.* **2003**, *372*, 394. Mpourmpakis, G.; Froudakis, G. E.; Andriotis, A. N.; Menon, M. *J. Chem. Phys.* **2003**, *119*, 7498. Mpourmpakis, G.; Froudakis, G. E.; Andriotis, A. N.; Menon, *Phys. Rev. B* **2003**, *68*, 125407.
(14) Chen, Z.; Hirsch, A.; Nagase, S.; Thiel, W.; Schleyer, P. v R. *J. Am. Chem. Soc.* **2003**, *125*, 15507.
(15) Sen, P.; Mitas, L. *Phys. Rev. B* **2003**, *68*, 155404.
(16) Menon, M.; Andriotis, A. N.; Froudakis, G. E. *Nano Lett.* **2002**, *2*, 301.
(17) Zhang, X.; Li, G.; Gao, Z. *Rapid Commun. Mass Spectrom.* **2001**, *15*, 1573. Zhang, X.; Li, G.; Xing, X.; Zhao, X.; Tang, Z.; Gao, Z. *Rapid Commun. Mass Spectrom.* **2001**, *15*, 2399.
(18) Li, G.; Zhang, X.; Tang, Z.; Gao, Z. *Chem. Phys. Lett.* **2002**, *359*, 203.
(19) Kumar, V.; Esfarjani, K.; Kawazoe, Y. In *Clusters and Nanomaterials*; Kawazoe, Y., Kondow, T., Ohno, K., Eds.; Springer Series in Cluster Physics; Springer-Verlag: Heidelberg, 2002; p 9.
(20) Müller, J.; Liu, B.; Shvartsburg, A. A.; Ogüt, S.; Chelikowsky, J. R.; Siu, K. W. M.; Ho, K.-M.; Gantefor, G. *Phys. Rev. Lett.* **2000**, *85*, 1666. Ballone, P.; Andreoni, W.; Car, R.; Parrinello, M. *Phys. Rev. Lett.* **1988**, *60*, 271. Majumder, C.; Kumar, V.; Mizuseki, H.; Kawazoe, Y. *Phys. Rev. B* **2001**, *64*, 233405. Shvartsburg, A. A.; Liu, B.; Lu, Z.-Y.; Wang, C.-Z.; Jarrold, M. F.; Ho, K.-M. *Phys. Rev. Lett.* **1999**, *83*, 2167.
(21) Kumar, V.; Kawazoe, Y. *Appl. Phys. Lett.* **2003**, *83*, 2677.
(22) Kresse, G.; Furthmüller, J. *Phys. Rev. B* **1996**, *55*, 111 69.

NL0498076

Variable Temperature STM/STS Investigations of Ag Nanoparticles Growth on Semiconductor Surfaces

S. SUTO[a], R. CZAJKA[b,c], S. SZUBA[b], A. SHIWA[a], S. WINIARZ[b], H. NAGASHIMA[a], H. KATO[a], T. YAMADA[d] AND A. KASUYA[c]

[a]Department of Physics, Tohoku University, Sendai 980-8578, Japan
[b]Faculty of Technical Physics, Poznan University of Technology
Nieszawska 13 A, 60-965 Poznań, Poland
[c]Center for Interdisciplinary Research, Tohoku University
Sendai 980-8578, Japan
[d]Institute of Physical and Chemical Research, Wako 351-0198, Japan

We have investigated the growth of Ag nanoparticles deposited on Si(111), H/Si(111)-(1×1) and Bi_2Te_3 substrates using a variable temperature scanning tunneling microscopy. These substrates are different as regards the model system for cluster and islands growth at the nanometer scale. Ag was evaporated onto the sample mounted at the scanning tunneling microscopy stage in vacuum of 10^{-10} Torr range during evaporation. The substrates were kept at different temperatures: −150°C, room temperature, and 300°C during the deposition process. In general, we have observed 3D growth mode up to several ML coverage. The density of clusters and their size were functions of the substrate's temperature during the deposition process — a higher density and a smaller size at −150°C were in opposition to the 300°C results — a lower density and a larger size. Low temperature depositions led to continuous layers above 10 ML coverage but the surface was covered by small Ag clusters of 1–2 nm in heights and 2–3 nm in diameters. The log-log graphs of height and projected diameter of Ag clusters revealed different slopes indicating different growth mechanisms at low and high temperatures. We obtained the value of $n = 0.25 \pm 0.02$, typical of the so-called droplet model of cluster growth, only at 300°C. Scanning tunneling spectroscopy measurements revealed clearly different I–V (and dI/dV vs. bias voltage) curves measured above clusters and directly above the substrate. In discussion, we compared our results to theoretically calculated density of states from other papers, finding conformity for partial density of states.

PACS numbers: 68.37.Ef, 68.47.Fg, 68.55.Ac

1. Introduction

It is a well-known fact that the epitaxy of thin metallic films is dependent on the early stage of nucleation [1]. Frequently, these films are composed of small discrete droplets (often named "clusters"), which grow, then coalesce into bigger droplets or islands, and finally create a complete layer. Both, the clusters and ultra thin films, exhibit new and specific physical properties due to their reduced dimensionality. Therefore, they have a wide and increasing number of scientific and commercial applications.

The substrates play a significant role in the film growth process. Semiconductors are mostly used as substrates to build integrated circuits. Si(100) or Si(111) represent substrates strongly interacting with adsorbents. This is a result of the presence of various dangling bonds at their surfaces [2]. Different passivation techniques were employed on silicon surfaces to make the surface less active and more uniform. One of such techniques is oxidation [3]. However, it is quite difficult to make the surface uniform as regards oxide thickness and its electronic properties. More recently, thin metallic nitride films have been used [4] to passivate the substrate or create a thin barrier layer before Cu plating, for example. One of the other methods is hydrogen termination using both the "dry method" in vacuum [5] and the so-called "wet method", by dipping the silicon substrate in HF or other solution containing both H and F ions [6 ,7]. The latter method gives a smooth surface with 1×1 reconstruction (as in bulk silicon) which weakly interacts with adsorbents. In this sense, substrate is closer to layered materials such as graphite (HOPG — highly oriented pyrolytic graphite), MoS_2 or Bi_2Te_3. The last material has been attracting considerable attention due to its potential application in the micro-fabrication of integrated thermoelectric devices [8].

Transition from two-dimensional (2D) to three-dimensional (3D) growth during Ag or Al/Si(111) 7×7 heteroepitaxy [9] is the main difference with the droplet growth on H–Si(111) 1×1 or Bi_2Te_3 substrates followed by the transition to the fractal coalescence of small metallic clusters.

As regards thin layer's growth mechanisms during the early stage of the growth, it is generally accepted that the growth of clusters follows scaling laws such as the size $R(t) \sim t^x$ [10, 11], where the exponent x depends on the type of growth mechanism. For the growth of three-dimensional clusters the predicted value of x is 1/4 and for two-dimensional clusters x is 1/2. However, the experimental results of Zuo [12] and our results, presented in this paper, show that the small metallic clusters undergo stages of liquid-like rapid coalescence alternating with nucleation and growth. Step-like growth behavior was observed which deviates from the continuous time dependence of cluster density and sizes predicted by the scaling theory.

Scanning tunneling microscopy (STM) [13] and spectroscopy (STS) are one of the most suitable analytical techniques to visualize nanostructures in real space (with STM) and to investigate their specific electronic properties (with STS).

The local density of electronic states (LDOS) can be measured using modulation techniques [14] or calculated [15] using current–voltage characteristics measured with the STM above the individual nanostructures or molecules or individual atoms. Quantum size effects (QSE) [16] or Coulomb blockade (CB) [17] effect may be observed as the sizes of small objects become comparable to the de Broglie wavelength of electrons confined within those objects. It was also shown that the STM/STS technique may be used for tracing both of the above-mentioned phenomena [18, 19].

In this paper we report our investigations of the growth of Ag nanoparticles deposited on H–Si(111) 1 × 1 and Bi_2Te_3 substrates and measured at different temperatures: −150°C (LT), room temperature (RT), and 300°C (HT). These substrates are different as regards the model system for cluster and islands growth at the nanometer scale. The first one represents substrates adsorbing with strong forces and the latter two interact with weak forces on deposits [12]. We also present our current imaging tunneling spectroscopy (CITS) measurements as well as DOS maps calculated using the Bando method [15] with $I-V$ curves measured by us.

2. Experimental

Ag was evaporated from OMICRON EFM3 source onto the sample mounted at the STM stage in vacuum of 10^{-10} Torr range. The pressure during evaporation, although slightly worse, was kept in the same range. The commercial variable temperature STM enabled us to change the sample's temperature between 125 K (using liquid nitrogen) and 600 K using sample holder with built in the boron nitride (BN) heater.

The "exposure", defined as a product of evaporation time and ion flux, was our main parameter of the evaporation rate. The ion flux, which constitutes a small but constant part of the atomic flux, was measured by a circuit built into the evaporation source. Assuming that the ion flux was kept constant, the exposure was directly proportional to the evaporation time and could be used in our data analysis according to the scaling theory. We used fluxes between 20 and 200 nA s which gave us the deposition rates between 0.025 and 0.25 ML per minute.

The Si(111) 7 × 7 substrate was prepared traditionally by flashing at about 1250°C for 10 seconds followed by the slow temperature fall between 900°C and 600°C.

The H–Si(111) 1 × 1 substrates were prepared using the chemical "wet" method which consists of many cleaning procedure steps to remove SiO_2 and finishes with the hydrogen termination in 40% NH_4F solution. The samples were finally rinsed with clean (Millipore Quality) water and transferred to UHV chamber. Then, H–Si(111) samples were annealed at about 200°C temperature for several hours.

The Bi_2Te_3 substrates were cleaved using a scotch tape, immediately transferred to UHV chamber, and then annealed for 2 hours at about 200°C.

The sample's temperature during the STM measurements was kept at the same level as it was during the evaporation, for example if the deposition was done at LT (−150°C) also STM/STS measurements were done at the same temperature. We started with low exposures of 10^3 nA s range to finish with 10^6 or 10^7 nA s. The sample in our setup was biased relatively to the tip. This means that the empty states were imaged for positive voltage, whereas the occupied ones were probed for negative bias. All STM topographic images were recorded in the constant current mode. We have used Ir cut tips as the STM probe.

3. Results

3.1. STM topography images

Figure 1 represents the STM images of substrates obtained with the atomic resolution. The image of 7 × 7 reconstruction on Si(111) shown in Fig. 1a is divided into two parts with negative and positive sample polarity, and illustrates the spatial distribution of highest occupied molecular orbital (HOMO) and lowest unoccupied molecular orbital (LUMO) states [2], respectively. Figure 1b shows 1 × 1 reconstruction of Si(111) surface obtained due to hydrogen passivation during the chemical wet procedure [6]. One can easily see the fcc hexagonal type structure

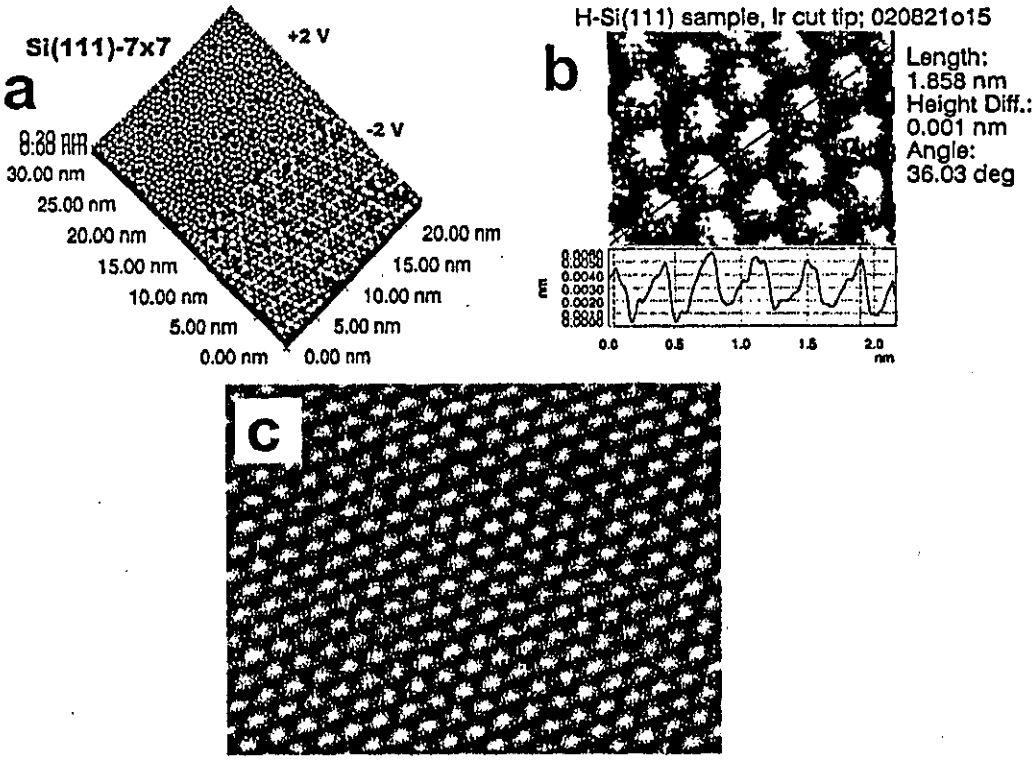

Fig. 1. STM images of: (a) Si(111) 7×7 substrate measured with positive bias (LUMO states) and negative bias (HOMO states); (b) H-passivated Si(111) substrate; (c) Bi_2Te_3 surface.

with 0.38 nm lattice constant. However, a relatively high number of point (or bigger) defects could also be observed. Finally, Fig. 1c shows the atomic resolution image of tellurium atoms' plane unveiled after the Bi_2Te_3 sample cleavage. The measured lattice constant is 0.44 nm and it is close to X-ray data value of 0.438 nm.

The typical images of silver clusters grown on H–Si(111) 1×1 substrate at four different temperatures from $-150°C$ up to 300°C with the exposure of 2×10^4 nA s are presented in Fig. 2. The amount of the Ag volume deposited on the substrate, in this case, was estimated with the help of WSxM software, and the values were 1.75 ± 0.25 ML, 0.75 ± 0.05 ML, 0.45 ± 0.05 ML and 0.35 ± 0.05 ML for substrate temperatures of $-150°C$, RT, 150°C, and 300°C, respectively. For coverage below 1 ML, we have observed cluster growth within the whole range of temperatures. In general, we have observed 3D growth mode up to several ML coverage. The density of clusters and their size were functions of the substrate's temperature during the deposition process — a higher density and a smaller size at LT was in opposition to the HT results — a lower density and a larger size. Qualitatively the same result, as regards the cluster density and its dimension one can observe in Fig. 3, where the STM images measured at LT, RT, and HT with the same deposited volume of Ag (1 ML and 5 ML) are collected. LT depositions led to continuous layers just above 10 ML coverage but the surface was covered by small Ag clusters of 1–2 nm in heights and 2–3 nm in diameters.

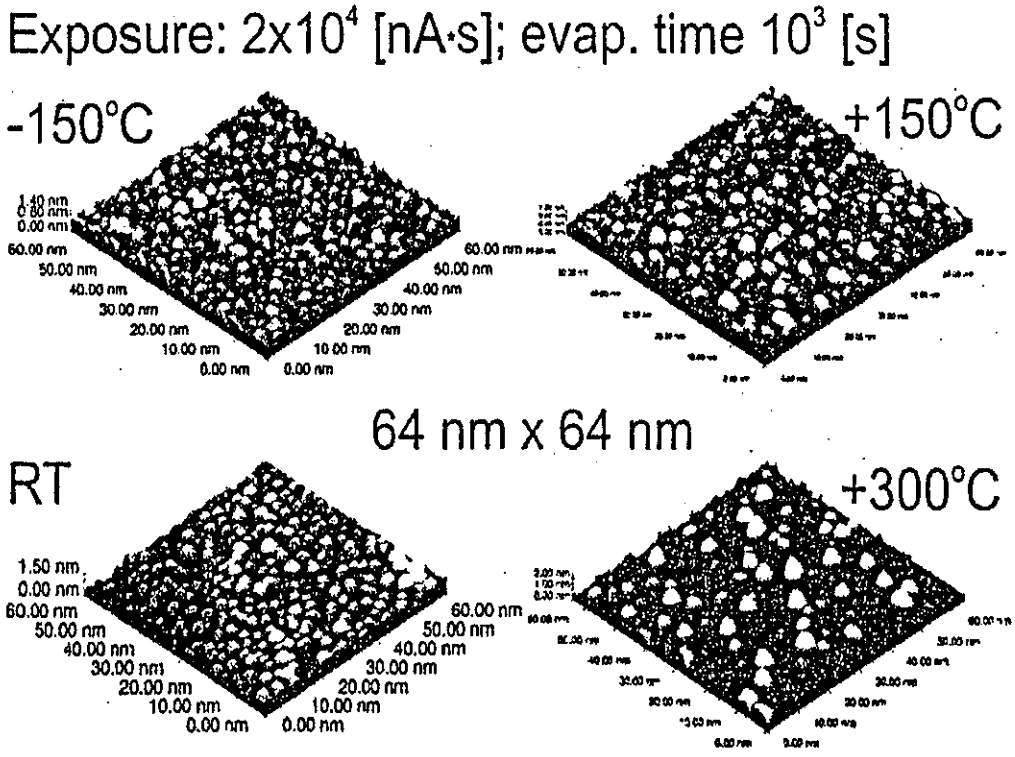

Fig. 2. The STM images of silver clusters grown on H–Si(111) 1×1 substrate at four different temperatures from -150 up to 300°C with the exposure of 2×10^4 nA s.

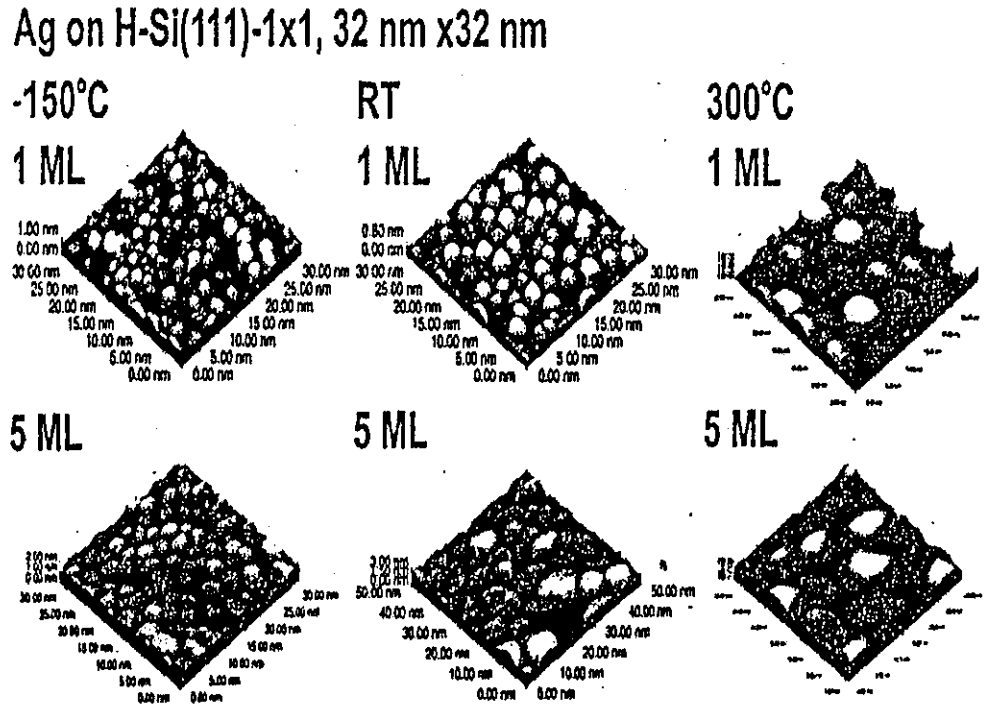

Fig. 3. The STM images measured at −150°C, RT, and 300°C with the same deposited volume of Ag (1 ML — the top row, and 5 ML — the bottom row).

3.2. Clusters' diameter and height plots versus exposure

The log–log graphs of height and projected diameter (as measured at the half of maximum height) of Ag clusters versus exposure were prepared to make the quantitative analysis of our data and compare our results with the predictions of the scaling theory [10, 11] and with the experimental data of other authors [12]. The obtained curves are presented in Fig. 4.

All the graphs of height and projected diameter of Ag clusters versus the exposure, besides the height plot at 300°C, have revealed complicated structures. The plots at LT may be divided into two parts: below and above 3×10^5 nA s (or 5×10^3 nA min as in Fig. 4's x-axis description). The apparent diameter is growing linearly in both ranges but with different slopes of 0.15 ± 0.03 and 0.30 ± 0.08, respectively (Fig. 4a and b). The height plot has a bell-type shape below 3×10^5 nA s exposure and linear type with 0.52 ± 0.08 slope above. The plots at RT may be divided into three parts. Below 6×10^4 nA s (1×10^3 nA min) exposure the diameter fluctuates between 2 and 5 nm, it becomes constant above this threshold up to 6×10^5 nA s (1×10^4 nA min) exposure and it linearly increases afterwards with the slope of 0.59 ± 0.06. The height versus exposure plot changes in the same way but with different values. Finally, at 300°C, the diameter is nearly constant (3.5 nm) up to 6×10^4 nA s (1×10^3 nA min) exposure and above it, it increases linearly with the slope of 0.21 ± 0.04. The height plot increases linearly within the whole range with the slope of 0.25 ± 0.02. Generally speaking, that data does not follow the scaling theory.

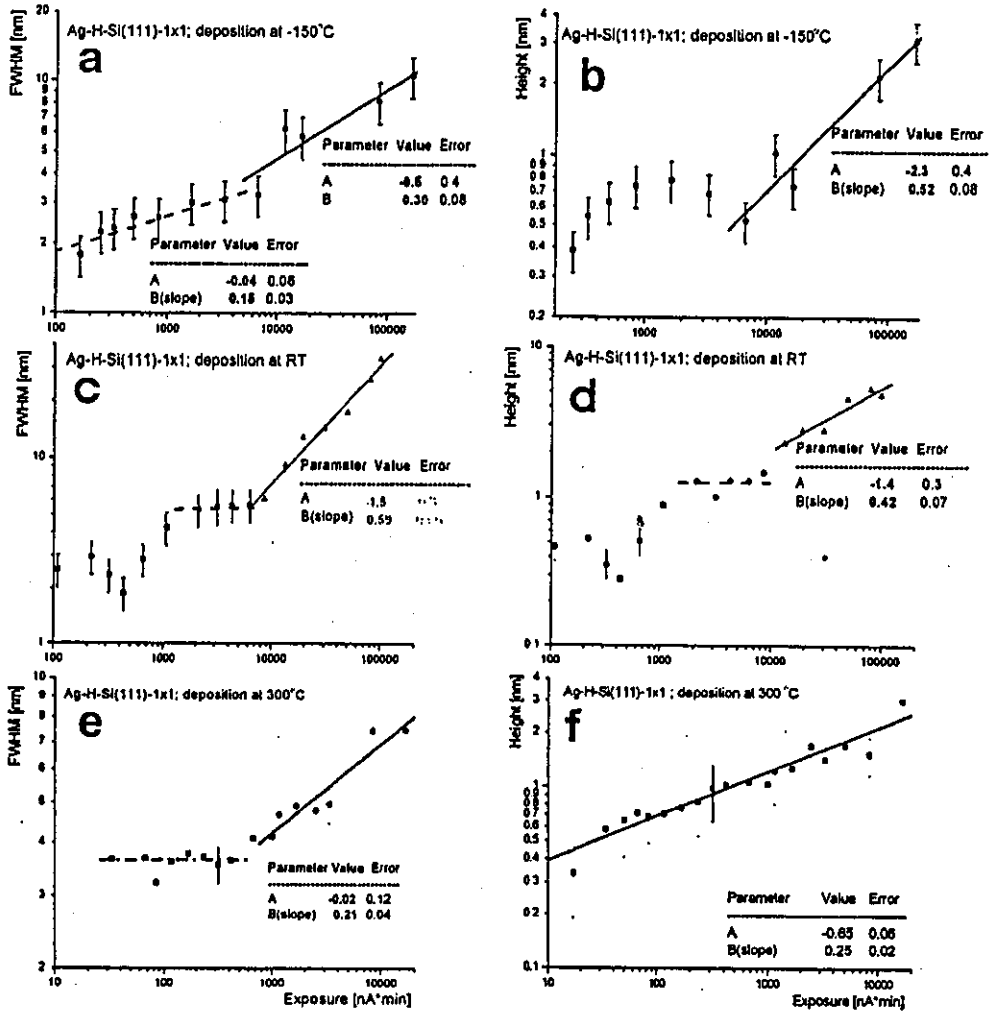

Fig. 4. The log–log graphs of height and projected diameter (as measured at the half of maximum height) of Ag clusters versus exposure (with [nA min] unit) measured at (a) and (b) −150°C, (c) and (d) RT and (e) and (f) 300°C.

3.3. Current imaging tunneling spectroscopy measurements

Scanning tunneling spectroscopy measurements were performed at RT and at LT conditions. However, the LT measurements suffered a conductivity decrease in the semiconducting substrate which diminished the measurements' sensitivity around the Fermi level within −3 to +3 range, as it is shown in Fig. 5.

Measurements at RT have revealed clearly different $I-V$ curves (and $\mathrm{d}I/\mathrm{d}V$ vs. bias voltage curves) measured above clusters and directly above the substrate. We performed current imaging tunneling spectroscopy (CITS) measurements, creating the tunnel current maps within a given range of bias voltage, from 1 up to a few volts, usually. The $I-V$ curves were measured at every point of the topographic image. Following these CITS measurements the density of states (DOS) was calculated from $I-V$ characteristics using the Bando method [15]. Figure 6

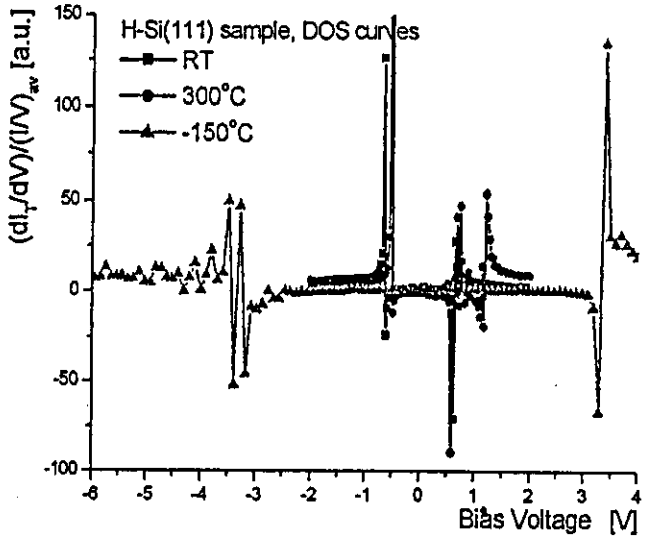

Fig. 5. The set of STS curves: I–V, $\mathrm{d}I/\mathrm{d}V$, and $(\mathrm{d}I/\mathrm{d}V)/(I/V)_{\mathrm{av}}$ vs. bias voltage measured above clean H–Si(111) 1 × 1 at LT, RT, and HT conditions.

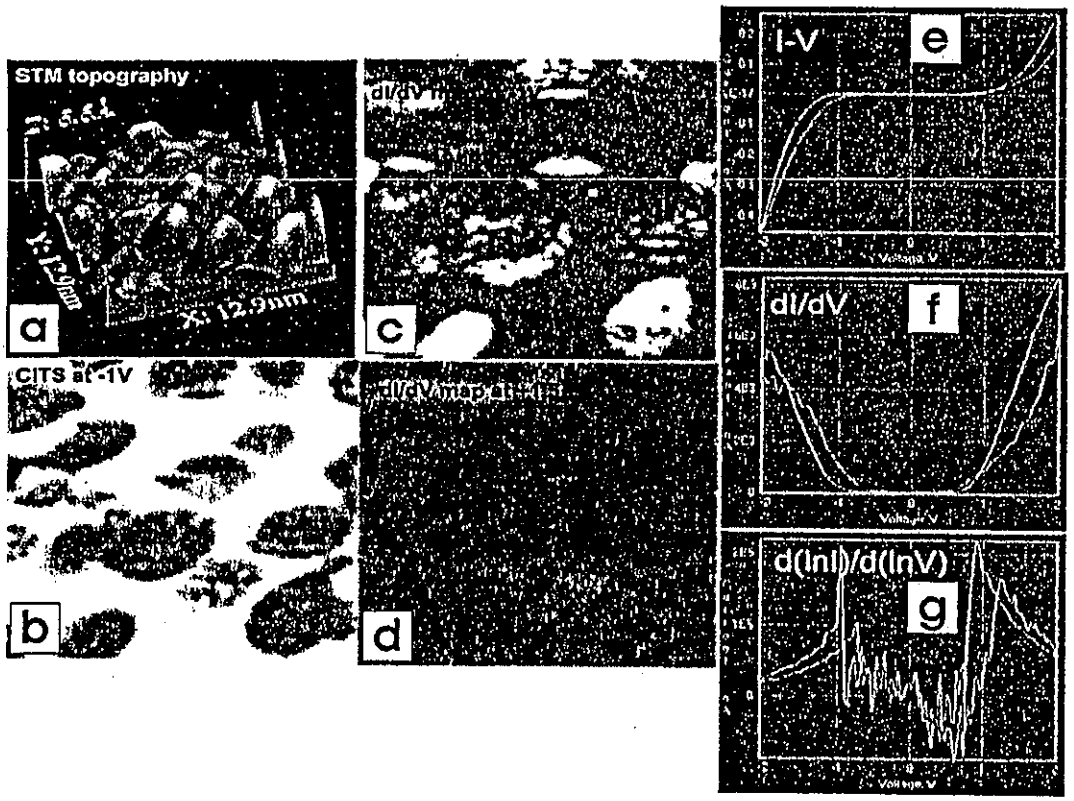

Fig. 6. The set of CITS results obtained on Ag clusters deposited on H–Si(111) 1 × 1 substrate: STM topography image (a), tunnel current map at –1 V bias polarization (b), the calculated spatial DOS distribution at the surface measured with two different bias polarizations –1 V (c) and +1.5 V (d), I–V curves (e), $\mathrm{d}I/\mathrm{d}V$ vs. bias voltage curve (f), and DOS vs. bias voltage (or energy) calculated using the Bando method (see the footnote on p. 297) (g).

shows a typical set of CITS results including topography image (Fig. 6a), tunnel current map at given bias polarization (Fig. 6b), spatial DOS distribution at the surface at two different bias polarizations (Fig. 6c and d), $I-V$ curves (Fig. 6e), dI/dV vs. bias voltage curve (Fig. 6f), and DOS vs. bias voltage (or energy) calculated using the Bando method* (Fig. 6g).

4. Discussion

4.1. Clusters' growth

The difference between the Ag or Al structures on Si(111) and H–Si(111) is distinct due to the strong and weak interactions with adsorbents on both substrates, respectively. For example, it is a well-known result that Ag on Si(111) creates the wetting layer first (with $\sqrt{3} \times \sqrt{3}$ reconstruction) and small islands then grow at the top of this layer [20]. We shall skip the Ag growth on Si(111) as it was discussed in many publications and we shall concentrate on our Ag cluster growth on H-passivated silicon.

The interaction between Ag and H terminated and therefore fully bonded Si is weak and Volmer–Weber (3-dimensional) growth of clusters is dominating as it is shown in Fig. 2. This cluster growth is a result of reduced, due to H-passivation, surface and interface energies. The Bi_2Te_3 substrate also belongs to lower energy surfaces. Therefore, nanometer-sized Ag clusters grow in droplet-like mode as it is shown in Fig. 7. This occurs when the binding energy of the condensate atoms or molecules to each other is greater than their binding energy to the substrate atoms.

According to the scaling laws the 3D cluster growth should scale as $R(t) \sim t^x$, with $x = 1/4$ and $x = 1/2$ in the case of 2D island growth. Our results, presented in Fig. 3, show that for short times of the clusters' growth or in the small size regime these scaling laws are not followed. These results are qualitatively in agreement with Zuo et al. TEM investigations [12]. At LT, the clusters' growth during the nucleation/growth stage follows the power law $R(t) \sim t^x$, with $x = 0.15$ up to 3.0×10^5 nA s exposure, so well below the expected 0.25 value from the scaling law, most probably due to decreased diffusion of atoms at the surface. However, the x value increases up to 0.30, which is close to 0.25 value within the experimental error, above 3.0×10^5 nA s exposure. This would suggest a smaller diffusion barrier of Ag on Ag than Ag on H–Si(111) surface at LT, as for this exposure nearly the whole surface is covered by Ag material. The height of clusters increases up to 3 monoatomic layers and reaches a maximum at about 1.5×10^5 nA s exposure, then it decreases to 2 monoatomic layers most probably due to secondary adsorption of Ag between existing clusters. The clusters' height increases again above 3.0×10^5 nA s exposure, however with the slope of 0.5 which is even higher than the slope for diameter and results in 3D growth of Ag clusters.

*The software was elaborated by S. Szuba.

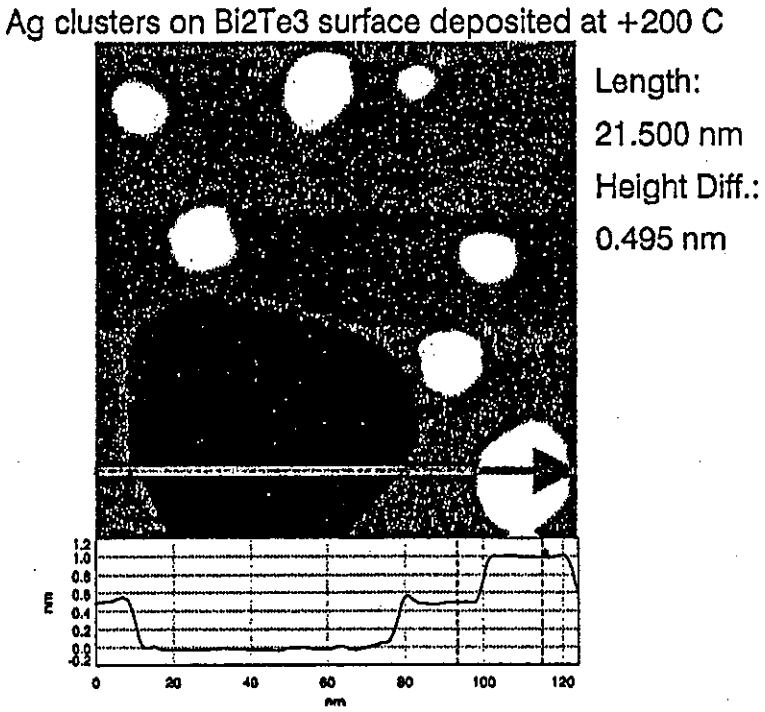

Fig. 7. The STM images of silver clusters grown on the Bi_2Te_3 substrate at 200°C. At the bottom — cross line section measured along the line marked at the topography image.

The clusters' diameter and height fluctuate up to 6×10^4 nA s exposure (about 1 ML of the deposited material) at RT on the level of 3 nm and 0.5 nm, respectively. These values become, respectively, (5 ± 1) nm and (1.25 ± 0.20) nm for exposures up to 6×10^5 nA s (up to 4 ML) while the density of clusters falls down. That means that the step-like growth of the Ag droplets took place at this range of exposures. Similar processes were observed for the diameter of a single droplet grown due to coalescence, as it was studied by Beysens et al. [21]. Above the threshold of 6×10^5 nA s exposure the diameter grows with the slope 0.59 ± 0.06 which is close to 0.50 value, typical of 2D island growth. That means that the late stage of growth takes place above the deposition of 4 ML of Ag at RT.

The diameter of Ag clusters is kept constant on the level of 3.6 ± 0.3 nm at high temperature conditions (300°C) while the height and density of clusters per area unit are increasing. This fact would suggest that clusters of constant and preferable diameter of 3.6 nm are created while their height increases from 2 up to 4 monoatomic thickness. The 3D growth of Ag clusters takes place above the threshold of 6×10^4 nA s exposure and both diameter and height increase with the slope close to or exactly 0.25 nm which is in agreement with the scaling law for this type of growth.

The model of the droplet growth may be divided into early and late stage regimes. The first one includes the formation of the first stable nuclei. Nearly all clusters have a smaller equilibrium concentration than supersaturation and thus

grow [10]. The cluster size distribution changes as a function of radius and time. During the late stage large clusters grow at the expense of smaller ones. This process is known as Ostwald ripening. According to this model the transition from early to late stage influences the cluster size distribution. Our experimental data received at HT conditions fit qualitatively the theoretical curves as it is seen in Fig. 8, where cluster size distribution diagrams corresponding to 0.2 ML and 5 ML deposition of Ag material are shown. Figure 8b reproduces the theoretical curves derived from Fick's second law of diffusion and Gibbs–Thomas equation [10].

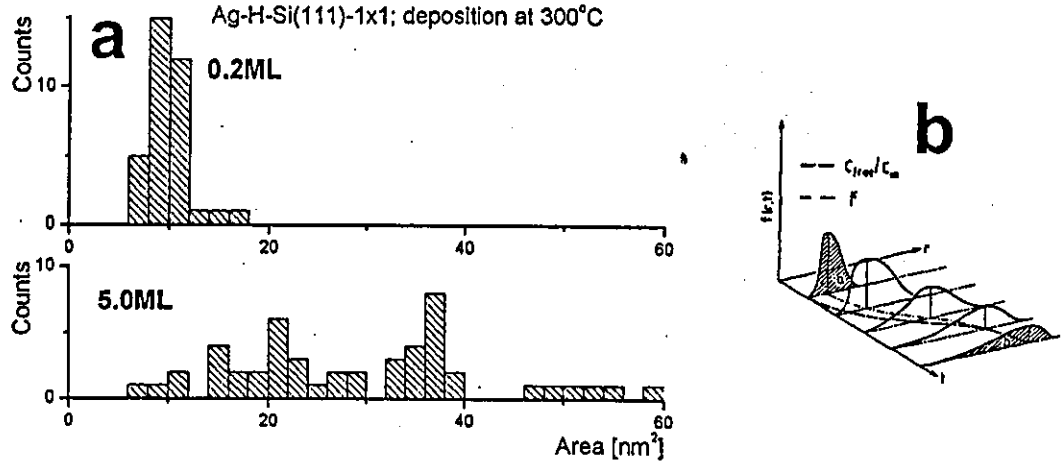

Fig. 8. (a) Clusters' size distribution diagrams corresponding to 0.2 ML and 5 ML deposition of Ag material. (b) The theoretical curves derived from Fick's second law of diffusion and Gibbs–Thomas equation [23].

Summarizing this part, we can say that we have found close agreement between the scaling law of early stage clusters' growth and experimentally observed data only at HT conditions.

4.2. Scanning tunneling spectroscopy on clusters

STM construction enables STS-type measurements by stopping the scanning at every or at any desired point on the investigated surface, switching off the feedback loop and performing the $I-V$ characteristics measurements. One may calculate or measure, using the modulation techniques, the dynamic conductivity ($\mathrm{d}I/\mathrm{d}V$ vs. bias polarization) which is more or less straightforwardly related to the local density of electronic states (LDOS) [22].

The electron charge density is explicitly present in the tunnel current formula as follows:

$$I \propto \int_0^{eV} \rho_s(r,E)\rho_t(r,-eV+E)T(E,eV,r)\mathrm{d}E, \qquad (1)$$

where $\rho_s(r,E)$ and $\rho_t(r,E)$ represent density of states for the sample and probe, respectively, evaluated at position r and for energy E measured against their in-

dividual Fermi's levels. $T(E, eV, r)$ is tunnel transmission probability for electrons with energy E at given bias polarization

$$T(E, eV) = \exp\left(-\frac{2s\sqrt{2m}}{\hbar}\sqrt{\frac{\phi_s + \phi_t}{2} + \frac{eV}{2} - E}\right), \quad (2)$$

where s — sample-probe distance, ϕ_s and ϕ_t — work functions for the sample and probe, respectively, $\hbar$ — Planck's constant/2π.

Usually DOS for metal tips (W, Pt/Ir, Au) are a smooth and continuous function of energy (or bias voltage), therefore any peculiarities seen in STM images must have originated in sample. One can expect such peculiarities when imaging small clusters or any other low-dimensional structures (nanowires, quantum dots). We have used the so-called Bando method [15] to calculate the LDOS from I–V measurements and create maps of the spatial distribution of LDOS. The individual I–V curves measured at the same point are noisy with some accidental jumps due to the extreme sensitivity of STM to vibration, and due to the fact that during I–V measurements the feedback loop, which controls the STM tip-sample distance, is switched off. Therefore, presented here I–V curves are averaged over few tens or even thousands of curves, usually. The LDOS maps were created using software developed by one of co-authors — S. Szuba.

Figure 5 shows a set of STS curves: I–V, $\mathrm{d}I/\mathrm{d}V$, and $(\mathrm{d}I/\mathrm{d}V)/(I/V)_{\mathrm{av}}$ vs. bias voltage measured above clean H–Si(111) 1 × 1 at LT, RT, and HT conditions. The DOS curves revealed the energy gap which is clearly seen (pronounced peaks) at RT and whose value is about 1.35 eV. The energy gap at 300°C was kept very close to the RT one (1.31 eV) which confirms that hydrogen termination is kept at this temperature. However, some additional states above the 0.63 eV and 1.22 eV appeared on the sample's occupied states side, with the highest one at 1.22 eV. We could observe the first strong DOS lines at LT conditions below –3.3 eV and above +3.3 eV due to decreased conductivity of semiconductor sample at LT. This fact limited our ability to investigate low energy (vs. Fermi energy) DOS states. The lines above 3.3 eV on both sides of Fermi energy (FE) level may be related to the emission from surface states and/or surface resonance as it was found by Arranz et al. [23] using photoelectron spectroscopy. However, the threshold is moved towards FE level by about 0.7 eV and we cannot exclude emission from the substrate related to the bulk Si transitions.

Figure 6 represents a typical set of our CITS data measured for Ag clusters grown on H–Si(111) 1 × 1 substrate after Ag exposure of 7 × 10^3 nA s at RT. The STM topography (Fig. 6a) reveals the presence of several clusters of 2 nm in average diameter. The current map (CITS) exhibits contrast between clusters of different sizes and the substrate (Fig. 6b). The DOS curves reveal the presence of energy gap of about 1.4 eV for the substrate and smaller clusters. The bigger clusters show an apparent gap of 0.8 eV. The smaller clusters are mostly 1 monoatomic layer high and the bigger ones are of two or three atomic layers in height. This fact would suggest that only double atomic or thicker clusters may

change the width of the observed gap due to the local electron charge transfer to the substrate. The calculated DOS map, using the Bando method, also reveals a similar type of contrast. This contrast changes with energy and one can observe the enhanced density of occupied states at clusters spots (e.g. at -1.0 eV) — Fig. 6c, and reduced density of states on empty states' side (e.g. at +1.7 eV) — Fig. 6d. Figures 6e–g represent I–V, $\mathrm{d}I/\mathrm{d}V$, $\mathrm{d}(\ln I)/\mathrm{d}(\ln V)$ vs. bias polarization curves and cross line profile of DOS map at above-mentioned bias polarization values, respectively. The I–V and other spectroscopic curves evaluate towards metallic type curves with the increasing Ag exposures.

CITS maps measured over the clean Bi_2Te_3 surface exhibited a contrast between different terraces or islands. The $\mathrm{d}I/\mathrm{d}V$ (~DOS) curves referred to those planes were compared with theoretically calculated DOS. We could conclude that curve measured above one of terraces is similar to DOS of Bi p orbital presented in Ref. [24]. Adequately the curve measured above different terraces resembles the DOS curve of Te-1 p orbital. This analysis allowed us to distinguish between bismuth and tellurium planes. The detailed analysis and data are reported by Winiarz et al. [25] in the same issue of *Acta Physica Polonica A*.

5. Conclusions

The growth of Ag clusters deposited on Si(111) 7 × 7 surface for small exposures depends strongly on the substrate temperature. The density of clusters was higher and the size was smaller at LT in opposition to the HT results — a lower density and a larger cluster's size. The log–log graphs of height and projected diameter of Ag clusters revealed different slopes (between 0.25 to 0.59) indicating different growth mechanisms at low and high temperatures. We obtained the value of $n = 0.25 \pm 0.02$, typical of the so-called droplet model of cluster growth, only at 300°C. The density of clusters was much smaller and their diameters were much bigger when the Ag clusters were grown on weakly interacting substrates as Bi_2Te_3.

Scanning tunneling spectroscopy measurements revealed clearly different I–V curves (and $\mathrm{d}I/\mathrm{d}V$ vs. bias voltage curves) measured above clusters and directly above the substrate. The I–V and other spectroscopic curves evolve from semiconductor type towards metallic type curves with increasing Ag thickness (above 2 ML).

CITS maps measurements enabled the evaluation of LDOS from I–V characteristics using the Bando method. The created maps of LDOS distribution showed variation of the LDOS with nanometer spatial resolution.

Acknowledgments

As regards Polish co-authors, this work was supported by the Ministry of Scientific Research and Information Technology (Project No. 2P03B 042 25).

References

[1] D. Walton, *J. Chem. Phys.* **37**, 2182 (1962).

[2] K. Takayanagi, Y. Tanishiro, M. Takahashi, S. Takahashi, *J. Vac. Sci. Technol. A* **3**, 1502 (1985).

[3] G.D. Wilk, Yi Wei, Hal Edwards, R.M. Wallace, *Appl. Phys. Lett.* **70**, 2288 (1997).

[4] R.N. Wang, J.Y. Feng, Y. Huang, *Appl. Surf. Sci.* **207**, 139 (2003).

[5] D. Gräf, M. Grundner, R. Schulz, L. Mühlhoff, *J. Appl. Phys.* **68**, 5155 (1990).

[6] G.S. Higashi, Y.J. Chabal, G.W. Trucks, K. Raghavachari, *Appl. Phys. Lett.* **56**, 656 (1990).

[7] T. Yamada, T. Inoue, K. Yamada, N. Takano, T. Osaka, H. Harada, K. Nishiyama, I. Taniguchi, *J. Am. Chem. Soc.* **125**, 8039 (2003).

[8] Gao Min, D.M. Rowe, *Solid State Electron.* **43**, 923 (1999).

[9] P. Sobotik, I. Ostadal, J. Myslivecek, T. Jarolimek, F. Lavicky, *Surf. Sci.* **482-485**, 797 (2001).

[10] M. Zinke-Allmang, L.C. Feldman, M.H. Grabov, *Surf. Sci. Rep.* **16**, 377 (1992).

[11] F. Family, P. Meakin, *Phys. Rev. Lett.* **61**, 428 (1988).

[12] J.M. Zuo, B.Q. Li, *Phys. Rev. Lett.* **88**, 255502 (2002).

[13] G. Binnig, H. Rohrer, *Helv. Phys. Acta* **55**, 726 (1982).

[14] R.J. Hamers, R.M. Tromp, J.E. Demuth, *Phys. Rev. Lett.* **56**, 1972 (1986).

[15] H. Bando, T. Shimitzu, Y. Aiura, Y. Haruyama, K. Oka, Y. Nishihara, *J. Vac. Sci. Technol. B* **14**, 1060 (1996).

[16] H. Frohlich, *Physica* **4**, 406 (1937).

[17] D.V. Averin, K.K. Likharev, *J. Low Temp. Phys.* **62**, 345 (1986).

[18] J.G.A. Dubois, J.W. Gerritsen, S.E. Shafranjuk, E.J.G. Boon, G. Schmid, H. van Kempen, *Europhys. Lett.* **33**, 279 (1996).

[19] P.J.M. van Bentum, R.T.M. Smokers, H. van Kempen, *Phys. Rev. Lett.* **60**, 2543 (1988).

[20] K.J. Wan, X.F. Lin, J. Nogami, *Phys. Rev. B* **47**, 13700 (1992).

[21] D. Beysens, C.M. Knobler, *Phys. Rev. Lett.* **57**, 1433 (1986).

[22] R.M. Feenstra, J.A. Stroscio, A.P. Fein, *Surf. Sci.* **181**, 295 (1987).

[23] A. Arranz, J.F. Sanchez-Royo, J. Avila, V. Perez-Dieste, P. Dumas, M.C. Asensio, *Phys. Rev. B* **65**, 075405 (2002).

[24] P. Larson, S.D. Mahanti, *Phys. Rev. B* **61**, 8162 (2000).

[25] S. Winiarz, R. Czajka, S. Suto, P. Łoś tak, S. Szuba, A. Kasuya, *Acta Phys. Pol. A* **104**, 389 (2003).

Vol. 104 (2003) *ACTA PHYSICA POLONICA A* No. 3-4

Proceedings of the 3rd International Symposium on Scanning Probe Spectroscopy, SPS'03

STM/STS Studies of Self-Organized Growth of Iron Silicide Nanocrystals on Vicinal Si(111) Surface

A. WAWRO[a,b], S. SUTO[c], R. CZAJKA[a,d] AND A. KASUYA[a]

[a]Center for Interdisciplinary Research, Tohoku University
Sendai 980-8578, Japan
[b]Institute of Physics, Polish Academy of Sciences
al. Lotników 32/46, 02-668 Warszawa, Poland
[c]Department of Physics, Graduate School of Science
Tohoku University, Sendai 980-8578, Japan
[d]Faculty of Technical Physics, Poznań University of Technology
Nieszawska 13A, 60-965 Poznań, Poland

The evolution of iron silicide structure grown by solid state epitaxy on Si(111) vicinal surface was investigated by scanning tunnelling microscopy. The reactions, which occur on the surface, are compared for two various Fe coverages: 0.33 and 2 monolayers. The annealing at 250°C does not enable substantial recovery of the surface ordering, deteriorated by Fe deposition at room temperature. The onset of 2×2 surface reconstruction is observed upon annealing at 400°C. A three-dimensional growth tendency of iron silicide crystallites on a bare Si(111) 7×7 surface was found at 700°C. In the case of 2 monolayer coverage crystallites nucleate along the edges of substrate terraces forming a regular array of nanometer size dots. Basing on atomically resolved spectroscopic effects and statistical considerations, structure of iron silicide nanocrystallites as well as Schottky-like character of the barrier at the interface between metallic crystallite and semiconducting substrate is deduced.

PACS numbers: 61.46.+w, 68.35.-p, 68.37.Ef, 81.10.Jt

1. Introduction

Iron silicide has attracted much attention because of the complexity of numerous compounds and serious expectations for practical applications [1]. De-

pending on the crystalline structure it reveals various properties: semiconducting (β-$FeSi_2$), metallic (α-$FeSi_2$, ε-FeSi) or ferromagnetic (Fe_3Si). Particularly the semiconducting phase is a very promising material for Si-based optoelectronic devices, because it has a narrow energy gap of 0.87 eV, which corresponds to the maximum transmission of the optical glass fibers. Moreover, compounds grown in the form of thin films reveal even wider group of structures, some of which have no counterpart in the bulk. The phases, which do not appear in a bulk material, are stabilized by the strains, generated by the lattice mismatch at the interface with the Si substrate. The grown structures are very sensitive to the various deposition methods: co-deposition by molecular beam epitaxy [2–7], reactive deposition epitaxy [8–10], solid state epitaxy [11–16] as well as to parameters which affect kinetic factors. Therefore, apparently the same growth conditions may result in substantially different phases displaying undesirable properties.

Iron silicide phase transition upon annealing is another contradictory issue. The phase transition temperature is affected by the film thickness, because the factors, which stabilize epitaxial phases, significantly depend on the interface structure [2, 3, 7, 9, 13, 15, 17–19].

The composition of the topmost atomic layer is also intensively discussed matter. It is generally accepted that the termination layer consists of Si atoms [11, 14, 20, 21], because they lower the surface energy of iron silicide. However, sparse experimental works and theoretical considerations reveal the presence of Fe atoms on the surface [22, 23].

The early stage formation of iron silicide was the aim of our investigations. The reactions, which occur upon low coverage Fe deposition onto Si(111) vicinal surface, activated by subsequent successive annealing, were studied with atomic resolution by means of scanning tunnelling microscopy (STM), supported by spectroscopic measurements. Our attention was also focused on the influence of vicinal structure of the substrate on surface diffusion, which affected the growth mode of iron silicide.

2. Experimental

Iron was deposited on silicon at room temperature in a UHV system at the base pressure in the low range of 10^{-10} Torr. The sample substrates were cut from commercial n-type Si(111) wafers (Sb doped, $\approx$ 1 Ω cm), misoriented by 1.2° in [–1 –1 2] direction. Clean surface was achieved through heating at 700°C for several hours and flashing at 1250°C up to 5 times, followed by cooling down at the rate lower than 1°C/s. Such thermal treatment resulted in the high quality surface showing 7×7 reconstruction with a negligible amount of defects and contamination. As a consequence of cutting misorientation the substrate surface had a terrace-like structure 800–1000 Å in width, separated by edge steps about 20 Å in average height. Iron was sublimated onto the substrate from a tungsten

basket typically at a rate of 5 Å/min. The deposition rates and the thickness were monitored by a quartz crystal microbalance. It was assumed that 1 monolayer (ML) corresponded to 1.2×10^{15} atoms/cm^2, i.e. average value of the low index surfaces of bcc Fe. The scanning tunnelling microscopy measurements were performed in the same vacuum system at room temperature directly after iron deposition and subsequent annealing for 10 min at: 250°C, 400°C, and 700°C. The STM tips were electrochemically etched from a tungsten wire (0.2 mm in diameter) and cleaned by annealing in the vacuum system. The sample was biased relatively to the tip in our setup. This means that the empty states were imaged for positive voltage, whereas the occupied ones were probed for negative bias. All STM topographic images were recorded in the constant current mode.

3. Results and discussion

The deposition of Fe on Si substrate deteriorates, in general, the reconstruction observed for clean surface. In the case of 0.33 ML Fe deposition, clusters of about one atomic monolayer in height and 1 nm in diameter randomly appear on the surface. Single atoms, irregularly aligned between them, are visible, however their unambiguous identification on the basis of the topographic image is questionable. Occasionally, small fragments of non-destroyed Si substrate with remnant 7 × 7 reconstruction are found. Upon deposition of 2 ML Fe larger agglomerates, of non-regular shape and few nanometers in diameter, are formed. The surface between them does not reveal the ordering typical of clean Si surface anymore. Results achieved for Fe are in contrast with an experiment performed in the same conditions for Au deposits. After deposition of Au submonolayer on Si(111) surface, small clusters nucleate mainly in the centres of both halves of the unit meshes [24]. A clear 7 × 7 substrate reconstruction visible between clusters suggests that the deposited Au does not react with Si. Therefore our findings allow an inference that the solid state reaction between the deposited iron and the silicon substrate proceeds intensively already at room temperature.

A short-range ordering of surface atoms becomes visible after annealing at 250°C. Three atoms' rings randomly distributed are the only regular objects encountered on the surface. However, their azimuthal planar orientation is identical, suggesting the influence of the Si substrate symmetry on their formation process. The distance between atoms, being members of a ring, equals to 6.6 Å, which is much more than the bonding length in the bulk Si (3.86 Å). Therefore the observed ordering cannot be considered as 1 × 1 reconstruction [4, 14, 25]. It rather correlates well with 2×2 reconstruction of ε phase [26], however this phase is not found upon annealing at higher temperatures. Thus the formation of the rings might be associated with the initial stage of (CsCl)FeSi phase growth, unambiguously identified after annealing at higher temperature.

Upon annealing at 400°C the long-range ordering of the surface is activated. The proceeding processes drastically depend on the amount of deposited material.